INTERNATIONAL JOURNAL OF HYDROGEN ENERGY 38 (2013) 3073–3086

Available online at www.sciencedirect.com

SciVerse ScienceDirect

journal homepage: www.elsevier.com/locate/he

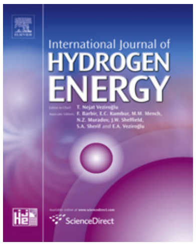

Diopside–Ba disilicate glass–ceramic sealants for SOFCs: Enhanced adhesion and thermal stability by Sr for Ca substitution

Allu Amarnath Reddy [a], *Dilshat U. Tulyaganov* [a,b], *Maria J. Pascual* [c], *Vladislav V. Kharton* [a], *Ekaterina V. Tsipis* [a], *Vladislav A. Kolotygin* [a], *José M.F. Ferreira* [a,*]

[a] *Department of Materials and Ceramics Engineering, University of Aveiro, CICECO, 3810-193 Aveiro, Portugal*
[b] *Turin Polytechnic University in Tashkent, 17, Niyazova Str., 100095 Tashkent, Uzbekistan*
[c] *Instituto de Cerámica y Vidrio (CSIC), C/Kelsen 5, Campus de Cantoblanco, 28049 Madrid, Spain*

ARTICLE INFO

Article history:
Received 14 October 2012
Received in revised form
3 December 2012
Accepted 11 December 2012
Available online 12 January 2013

Keywords:
Sintering
Coefficient of thermal expansion
Thermal stability
Interaction
Interconnect

ABSTRACT

This article reports on the influence of strontium for calcium substitution in diopside–Ba disilicate glass–ceramics on stabilization thermal parameters and improvement adhesion to interconnect material of SOFCs. Sr replaced 10, 20, 30 and 40% of Ca in the $Ca_{0.9}MgAl_{0.1}La_{0.1}Si_{1.9}O_6$ component of the parent glass having the following composition, mol.%: 22.14 CaO, 24.60 MgO, 0.52 BaO, 1.23 Al_2O_3, 1.23 La_2O_3, 47.79 SiO_2, 1.69 B_2O_3, 0.79 NiO. ^{29}Si–MAS–NMR and ^{27}Al MAS–NMR spectra of the glasses revealed irrelevant chemical shifts for silicon and aluminum atoms upon changing the SrO content. T_g decreased and coefficient of thermal expansion (CTE) increased by Sr for Ca substitution in pyroxene glasses. Additionally SrO-containing glasses exhibited a viscosity of $\sim 10^6$ dPa s at 900 °C, which is suitable for joining of SOFC metallic/ceramic components by glass/glass–ceramic sealing upon stack hermetization. Glass–ceramics revealed long term (up to 1000 h) thermal stability at 900 °C and suitable CTE values $(10.0–11.3) \times 10^{-6}\ K^{-1}$, high electrical resistivity, good adhesion and minimal reactivity with SOFC components.

Copyright © 2012, Hydrogen Energy Publications, LLC. Published by Elsevier Ltd. All rights reserved.

1. Introduction

Fuel cells are the most efficient technology to convert chemical energy to electricity and thus could have a major impact on reducing fossil fuel consumption and CO_2 emissions. The United States of America (USA) has been leading efforts at increasing the performance of fuel cells especially SOFCs, one type of electrochemical device which has received and continues to receive considerable attention, through the DOE Office of Fossil Energy's SECA program. Among different designs of SOFC, flat plate (planar) design SOFCs become the most promising due to their easier fabrication, improved performance and high power density relative to other designs. However, these electrochemical cells are still limited by the mechanical behavior of hermetic seals and remain a major challenge in advancing this emerging technology [1–4].

In planar SOFCs, gas-tight seals must be formed along the edges of each cell and between the fuel cell stack and gas manifolds to perform at high efficiency. The sealant or sealants must meet the thermal, mechanical, physical, chemical, but also the electrical requirements. The most common sealing materials for SOFC are glasses or glass–ceramics and have been shown to operate in fuel cells for more than 1000 h with no significant degradation [2,3,5]. A principal advantage

---

* *Corresponding author*. Tel.: +351 234 370242; fax: +351 234 370204.
E-mail address: jmf@ua.pt (J.M.F. Ferreira).

0360-3199/$ – see front matter Copyright © 2012, Hydrogen Energy Publications, LLC. Published by Elsevier Ltd. All rights reserved.

http://dx.doi.org/10.1016/j.ijhydene.2012.12.074

of glass seals is that the glass composition can be tailored to optimize the properties like CTE, mechanical strength, electrical resistance, etc. However, for glass or glass–ceramic seals, the challenges lie not only in the bulk properties, but also in establishing stable sealing interfaces without forming undesirable phases over long periods of time (up to 40,000 h) under real fuel cell operating conditions [2,3,5]. For example alkali ions or residual water in some glass compositions significantly increase the vaporization of chromium from the interconnect [6] and reduce the SOFC efficiency.

While designing a suitable and compliant seal for SOFC or other high temperature electrochemical applications the chemical composition of glass should be chosen considering: (i) the role of each chemical constituent in the glass toward rendering the thermal and chemical stability along with mechanical integrity to the seal in hostile high temperature working environment, including minimum surface diffusion and poisoning phenomena; (ii) the various thermal and chemical environments to which the seal will be exposed during its operation, and; (iii) basic requirements such as good electrical insulating properties. Thus the glass compositions investigated in our previous studies [7–11] were designed in the primary crystallization field of diopside owing to their high chemical resistance, good sintering ability and relatively high coefficients of thermal expansion (CTE). A minor amount of B_2O_3 was added along with rare-earth oxides in order to tailor the viscosity and flow behavior. The glass–ceramic seals demonstrated high mechanical properties, phase stability at elevated temperatures, good wetting abilities and minimal chemical interaction with other SOFC components. However, thermal stability of these glass–ceramic seals during long term operation is still a matter of concern. Therefore, further experimentation is required in terms of tailoring glass chemistry so as to achieve a stable seal with appropriate CTE matching and minimal reactivity with SOFC components during long run. This can be achieved via reducing BaO content since BaO reacts with chromium oxides from the metallic interconnect under oxidizing environment. This interaction is highly detrimental for the SOFC stack. For example, significant content of BaO in the glasses can lead to formation of $BaCrO_4$ on the sealant surfaces due to the transport of volatile Cr-containing species, such as CrO_3 or $CrO_2(OH)_2$ [12]. The high coefficients of thermal expansion (CTE) of $BaCrO_4$ ($\sim 18 \times 10^{-6}$ K^{-1}), contributes to the physical separation of the sealing glass interconnects where the CTEs are $(10–13) \times 10^{-6}$ K^{-1} [12].

The literature survey evidenced that changing the thermal properties might be achieved by introducing SrO oxide in the silicate glass network. Ojha et al. [13] reported that SrO modified the network of Al_2O_3–B_2O_3–SiO_2–La_2O_3 glasses resulting in CTE 9×10^{-6} K^{-1}. Kumar et al. [14] studied the MgO/SrO-based borosilicate glasses and observed that SrO containing glasses exhibited higher CTE in comparison to MgO-based glasses. Mahapatra et al. [15] developed SrO–La_2O_3–Al_2O_3–SiO_2 (SABS-0) based glass with all the desired thermo physical properties. However, SABS-0 glass still needs to be tested in actual SOFC cells for long term under realistic dual atmosphere conditions. Kaur et al. [16] studied SrO/BaO–B_2O_3–La_2O_3–SiO_2 system and reported that SrO contain glass seals have shown high hermeticity and structural integrity with Crofer 22APU even after prolonged heat-treatment duration of 750 h at 850 °C whereas BaO glass seal exhibited substantial number of pores after prolonged heat-treatment. In a more recent study, Sherma et al. [17] evaluated SrO–BaO based aluminosilicate glasses with P_2O_5 as a nucleating agent and claimed that Ba_2SiO_4, $BaAl_2Si_2O_8$, and Sr_2SiO_4 crystalline phases developed at 800 °C were not detrimental for high temperature sealing applications.

The very promising glass composition $Ca_{0.9}MgAl_{0.1}La_{0.1}Si_{1.9}O_6$ reported in our previous study [10] was adopted as the starting point for synthesis of two different series of glasses by introducing different concentrations of magnesium orthosilicate (Mg_2SiO_4) and barium disilicate ($BaSi_2O_5$) [11]. The glass with the lowest BaO content (0.52 mol.%) demonstrated better adhesion to the interconnect material compared to other compositions. However, CTE of the parent glass was significantly lower than that of the glass–ceramics. In the present study new series of glasses was developed by partial substitution Sr for Ca in the same composition aiming to tailor CTE of parent glass and crystallized material. This study also aims at improving the wetting behavior of the sealants via reducing viscosity of the glasses in the deformation temperature interval and achieving stable thermo-mechanical properties of sintered glass-powder compacts.

2. Experimental procedure

2.1. Synthesis of glasses and glass–ceramics

Partial substitution of Sr for Ca was performed on molar basis in the $Ca_{0.9}MgAl_{0.1}La_{0.1}Si_{1.9}O_6$ component of the parent glass Di–Ba-1 (designated as Sr-0). Sr replaced 10, 20, 30 and 40% of Ca resulting in four new glasses Sr-0.1, Sr-0.2, Sr-0.3, and Sr-0.4, respectively. The chemical compositions of the experimental glasses are presented in Table 1. High purity powders of SiO_2 (>99.5%), $CaCO_3$ (>99.5%), $MgCO_3$ (BDH chemicals, UK, >99%), $BaCO_3$ (Sigma Aldrich, 99.9%), Al_2O_3 (Sigma Aldrich, >98%), La_2O_3, $SrCO_3$ (Sigma Aldrich, 99.9%), H_3BO_3 (>99.5%) and NiO (Sigma Aldrich, 99%) were used. Homogeneous batch mixtures of ~100 g (Table 1), obtained by ball milling were preheated at 1100 °C for 5 h for decarbonization and then melted in Pt crucibles at 1580 °C for 2 h, in air. More experimental details were

Table 1 – Nominal batch compositions of the glasses.

Glass	CaO	MgO	BaO	SrO	Al_2O_3	La_2O_3	SiO_2	B_2O_3	NiO
Sr-0.0									
wt.%	21.09	16.84	1.36	0.00	2.13	6.81	48.77	2.00	1.00
mol.%	22.14	24.60	0.52	0.00	1.23	1.23	47.79	1.69	0.79
Sr-0.1									
wt.%	18.36	16.5	1.36	4.24	2.09	6.67	47.79	2.00	1.00
mol.%	19.67	24.58	0.53	2.46	1.23	1.23	47.77	1.73	0.80
Sr-0.2									
wt.%	15.74	16.17	1.36	8.31	2.04	6.53	46.84	2.00	1.00
mol.%	17.19	24.56	0.54	4.91	1.23	1.23	47.75	1.76	0.82
Sr-0.3									
wt.%	13.23	15.85	1.36	12.22	2.00	6.40	45.94	2.00	1.00
mol.%	14.73	24.54	0.55	7.36	1.23	1.23	47.73	1.79	0.84
Sr-0.4									
wt.%	10.81	15.54	1.36	15.98	1.97	6.28	45.07	2.0	1.00
mol.%	12.26	24.52	0.56	9.81	1.23	1.23	47.71	1.83	0.85

described elsewhere [4,11]. The amorphous nature of glasses was confirmed by X-ray diffraction (XRD) analysis (Rigaku Geigerflex D/Max, Tokyo, Japan; C Series; Cu K_α radiation; 2θ range 10°–80°; step 0.02° s^{-1}).

Rectangular bars with dimensions of 4 mm × 5 mm × 50 mm were prepared by uniaxial pressing (80 MPa). In order to study the stability of shrinkage, density, mechanical strength and crystalline phase assemblages in glass–ceramics sealants after prolonged usage in SOFC stack the resultant glass–ceramics were sintered at 900 °C temperature for 1 h, 250 h, 500 h and 1000 h at 5 K min^{-1}. The linear shrinkage during sintering was calculated from the difference in the dimensions between the green and the sintered bars. Archimedes' method (i.e., immersion in diethyl phthalate) was employed to measure the apparent density of the sintered glass–ceramics. The mechanical properties were evaluated by measuring the three-point bending strength of rectified parallelepiped bars of sintered glass–ceramics (Shimadzu Autograph AG 25 TA, Columbia, MD; 0.5 mm min^{-1} displacement). The values of CTE for glasses and glass–ceramics (GCs) were obtained from dilatometry measurements carried out on prismatic samples with a cross section of 4 mm × 5 mm (Bahr Thermo Analyze DIL801 L, Hullhorst, Germany; heating rate 5 K min^{-1}).

2.2. *Structural characterization of glasses*

^{29}Si magic angle spinning (MAS) nuclear magnetic resonance (NMR) spectra were recorded on a Bruker ASX 400 spectrometer operating at 79.52 MHz (9.4 T) using a 7 mm probe at a spinning rate of 5 kHz. The pulse length was 2 μs and 60 s delay time was used. Kaolinite was used as the chemical shift reference. ^{27}Al MAS–NMR spectra were recorded on a Bruker ASX 400 spectrometer operating at 104.28 MHz (9.4 T) using a 4 mm probe at a spinning rate of 15 kHz. The pulse length was 0.6 μs and 4 s delay time. $Al(NO_3)_3$ was used as chemical shift reference. ^{11}B MAS–NMR spectra were recorded on a Bruker ASX 400 spectrometer operating at 128.36 MHz (9.4 T) using a 4 mm probe at a spinning rate of 12 kHz. The pulse length was 3.6 μs and 2 s delay time was used. H_3BO_3 was used as the chemical shift reference.

2.3. *Thermal analysis of glasses and study of their crystallization kinetics*

The sintering behavior of the glass powders was investigated using a side-view hot stage microscope (HSM) EM 201 equipped with image analysis system and 1750/15 Leica electrical furnace. The detailed experimental procedure was previous described [4,11]. The temperatures corresponding to the characteristic viscosity points (first shrinkage, maximum shrinkage) were obtained from the photographs taken during the hot-stage microscopy experiment following Scholze's definition [18,19].

The values of the glass transition temperature (T_g), crystallization onset temperature (T_c) and peak temperature of crystallization (T_p) were obtained by differential thermal analysis (DTA) using a Setaram LabSys TG-DTA16 instrument (Setaram Instrumentation, France) calibrated in the temperature range 25–1000 °C. The measurements were performed using powdered glass samples (50 mg) in an alumina crucible and α-alumina powder as reference at a heating rate of 5 K min^{-1}.

2.4. *Crystalline phase evolution in glasses*

The amorphous nature of glasses and qualitative along with quantitative analysis of crystalline phases in the GCs (crushed to particle size <45 mm) was made by XRD analysis using a conventional Bragg–Brentano diffractometer (Philips PW 3710, Eindhoven, The Netherlands) with Ni-filtered Cu–K radiation. The quantitative phase analysis of GCs was made by combined Rietveld–R.I.R (reference intensity ratio) method. 10 wt.% corundum (NIST SRM 676a) was added to all the GC samples as an internal standard, as reported elsewhere [4,11].

2.5. *Joining behavior and chemical interactions between electrolyte/seal and interconnect/seal diffusion couples*

To investigate the adhesion and chemical interactions of the glasses with SOFC components, wetting experiments between glasses (powder)–solid electrolyte (8 mol.% yttria-stabilized zirconia – 8YSZ, Tosoh) and glass-interconnect (Sanergy HT) were carried out. The glass powders, 40% solid content mixed with 5 vol.% solution of polyvinyl alcohol (PVA) prepared by dissolution of PVA in warm water, were deposited on YSZ electrolyte and on Sanergy HT by slurry coating. The diffusion couples were heated to 900 °C with a relatively slow β of 2 K min^{-1} and kept at that temperature for 1 h. Heat treatment was performed without applying any dead load. A similar procedure was used to prepare Sr-0.3/8YSZ diffusion couples used for the electrical measurements in order to test possible degradation processes in the course of annealing at SOFC operation temperature. In the latter case, porous Pt electrodes were deposited onto both GC and 8YSZ surfaces, and then fired at 870–880 °C during 15 min.

2.6. *Microstructural and electrical characterization*

Microstructural observations were made on polished surfaces of the sintered glass powder compacts (chemically etched by immersion in 2 vol.% HF solution for a duration of 2 min) by scanning electron microscopy (SEM; SU-70, Hitachi) with energy dispersive spectroscopy (EDS; Bruker Quantax, Germany) to study the distribution of elements in the crystals and along the glass–ceramics-interconnect diffusion couples.

The equipment and procedures used for testing of electrical properties of the glass–ceramic sealants sintered at 900 °C for 1000 h, oxygen permeability of dense GCs disks and their ion transference numbers were described elsewhere [7,10,11,20]. The total conductivity (σ) was determined by AC impedance spectroscopy using HP4284A and Gamry PCI4/750 instruments; the measurements were performed as function of temperature and time at 620–850 °C in flowing atmospheric air, dry Ar, argon humidified at room temperature, and 10% H_2–90% N_2 gas mixture. The water vapor partial pressures, determined by a Jumo humidity transducer in air, dry Ar, and humidified Ar flow, were 0.006 atm, $<10^{-4}$ atm and 0.03 atm, respectively. The ion transference numbers, which show the contribution of all mobile ions to the total conductivity, were assessed under air/10% H_2–90% N_2 gradient at 850 °C. In all cases, porous Pt electrodes deposited onto the surfaces of dense GC disks or bars were used; the partial pressures of oxygen and water vapor in the gas mixtures were controlled

Table 2 – Density (g cm^{-3}), molar volume (MV) (cm^3 mol^{-1}), excess molar volume (EMV) (cm^3 mol^{-1}) and CTE (±0.1 × 10^{-6} K^{-1}) (200–500 °C) of glasses.

Glass	Density	MV	EMV	CTE
Sr-0.0	2.990 ± 0.003	19.69 ± 0.02	0.75 ± 0.02	7.1
Sr-0.1	3.045 ± 0.006	19.72 ± 0.04	0.65 ± 0.04	10.0
Sr-0.2	3.088 ± 0.001	19.82 ± 0.01	0.62 ± 0.01	11.3
Sr-0.3	3.134 ± 0.005	19.92 ± 0.03	0.57 ± 0.03	11.2
Sr-0.4	3.167 ± 0.005	20.06 ± 0.03	0.59 ± 0.03	10.2

employing 8YSZ solid-electrolyte sensors and Jumo humidity transducers, respectively.

3. Results

3.1. *XRD analysis and thermal properties*

All the five glass compositions were prone for easy casting after 2 h of melting at 1580 °C, resulting in homogeneous and transparent glasses. With respect to the color, the glasses exhibited dark honey color due to the presence of NiO. The XRD amorphous nature of the quenched glasses and frits was confirmed by XRD analysis.

The density and molar volume of glasses (Table 2) increased with additions of SrO. The CTE of the glasses varied between 7.1 and 11.3 × 10^{-6} K^{-1} with the highest value observed for Sr-0.2 glass while Sr-0 glass featured the lowest value.

T_g of glasses presented in Table 3 were obtained from the DTA thermographs (Fig. 1a and b) as the mid-point of the endothermic dip. Heating rate of 20 K min^{-1} was used since T_g could not be accurately recorded at 5 and 10 K min^{-1}.

3.2. *Structure of glass: MAS–NMR*

Fig. 2a shows ^{29}Si MAS–NMR spectra of the glass samples. All spectra had a broad peak centered at 81 ppm indicative of Q^2 silicate species, with Q^0, Q^1, Q^3 and Q^4 being below detectable levels. The chemical shift of the peak is invariant with increasing Sr substitution for Ca in the present glasses. Fig. 2b shows ^{27}Al MAS–NMR spectra of the glass samples, all of which had a broad, slightly asymmetric peak with a tail toward more negative ppm indicating existence of ^{IV}Al, ^{V}Al and ^{VI}Al coordination. However, the signals originated from ^{IV}Al species at 55 ppm are dominating making ambiguous existence of ^{V}Al and ^{VI}Al groups. Fig. 2c shows ^{11}B MAS–NMR spectra of the glass samples, all of which had a broad resonance bands observed within the chemical shift range between 10 and −35 ppm. The peaks were centered at ca. −19, −14 and −9 ppm indicative of the majority of the boron atoms in three fold coordination, i.e. in the form of BO$_3$ triangles [21].

Table 3 – Thermal parameters measured from DTA and HSM (°C).

	Sr-0.0	Sr-0.1	Sr-0.2	Sr-0.3	Sr-0.4
$T_g \pm 2$	753	744	744	744	748
$T_{FS} \pm 8$	770	767	772	773	781
$T_{MS1} \pm 5$	837	831	835	847	848
$T_{MS2} \pm 5$	882	892	902	913	916
$T_C \pm 2$	844	850	859	876	883
$T_P \pm 2$	883	891	898	912	917
S_c (=$T_c - T_{MS}$)	7	19	24	29	35
$T_D \pm 5$	900	880	877	869	875
$T_S \pm 5$	–	–	–	1213	900
$T_{HB} \pm 8$	1305	1280	1258	1229	1207
$T_F \pm 10$	1341	1327	1290	1260	1228
A/A_0 at $T_{MS1} \pm 0.02$	0.65	0.68	0.64	0.65	0.67

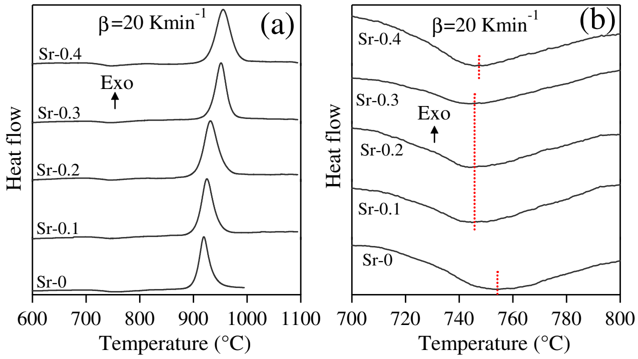

Fig. 1 – DTA thermographs of investigated glasses at 20 K min^{-1} within different temperature intervals: (a) 600–1100 °C; (b) 700–800 °C.

3.3. *Sintering and crystallization behavior: DTA and HSM*

Fig. 3 shows variation in the relative area and heat flow with respect to temperature as gained from HSM and DTA measurements, respectively at a heating rate of 5 K min^{-1}. Table 3 summarizes the values of the temperature of first shrinkage (T_{FS}; log η = 9.1 ± 0.1; η is viscosity in dPa s), temperature for maximum shrinkage (T_{MS}; log η = 7.8 ± 0.1), temperature for deformation (T_D; log η = 6.3 ± 0.1), temperature for half-ball (T_{HB}; log η = 4.1 ± 0.1), temperature for flow (T_F; log η = 3.4 ± 0.1), and ratio of the final area/initial area of the glass powder compact (A/A_0), as obtained from the HSM data at T_{MS} (Fig. 3), along with temperature for onset of crystallization (T_c), peak temperature of crystallization (T_p) as received from DTA of the glasses. The data as obtained from DTA and HSM (β = 5 K min^{-1}) pertaining to

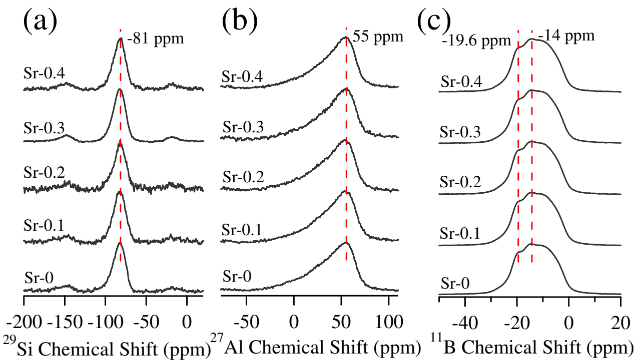

Fig. 2 – MAS–NMR spectra for (a) ^{29}Si; (b) ^{27}Al; and (c) ^{11}B Nuclei.

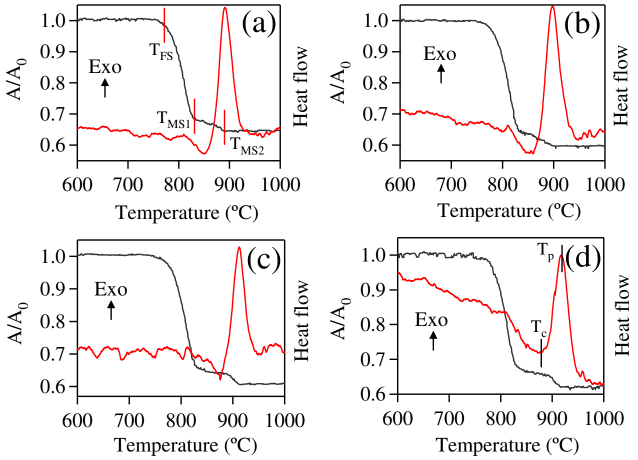

Fig. 3 – DTA–HSM thermographs of the investigated glasses at 5 K min^{-1}: (a) Sr-0.1; (b) Sr-0.2; (c) Sr-0.3; and (d) Sr-0.4.

sintering and devitrification behavior of glasses that allow observation of the following trends:

1. With the initial replacement of SrO for CaO T_{FS} decreased from 770 to 761 °C whilst increased from 761 to 781 °C with further replacement.

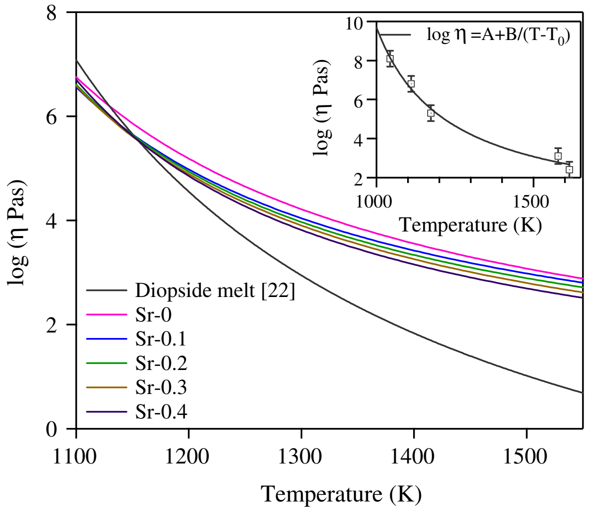

Fig. 5 – Comparison of viscosity curves with diopside melt viscosity curve (log $\eta = -4.27 + 3961K/(T - 751K)$ [22]). Inset figure represents the viscosity curve derived from HSM characteristic viscosity points for Sr-0 glass.

2. All glasses exhibited two stage of sintering: the first sintering stage is accomplished at T_{MS1} while the second one at T_{MS2}. In all the compositions $T_{MS1} < T_c$, so that sintering

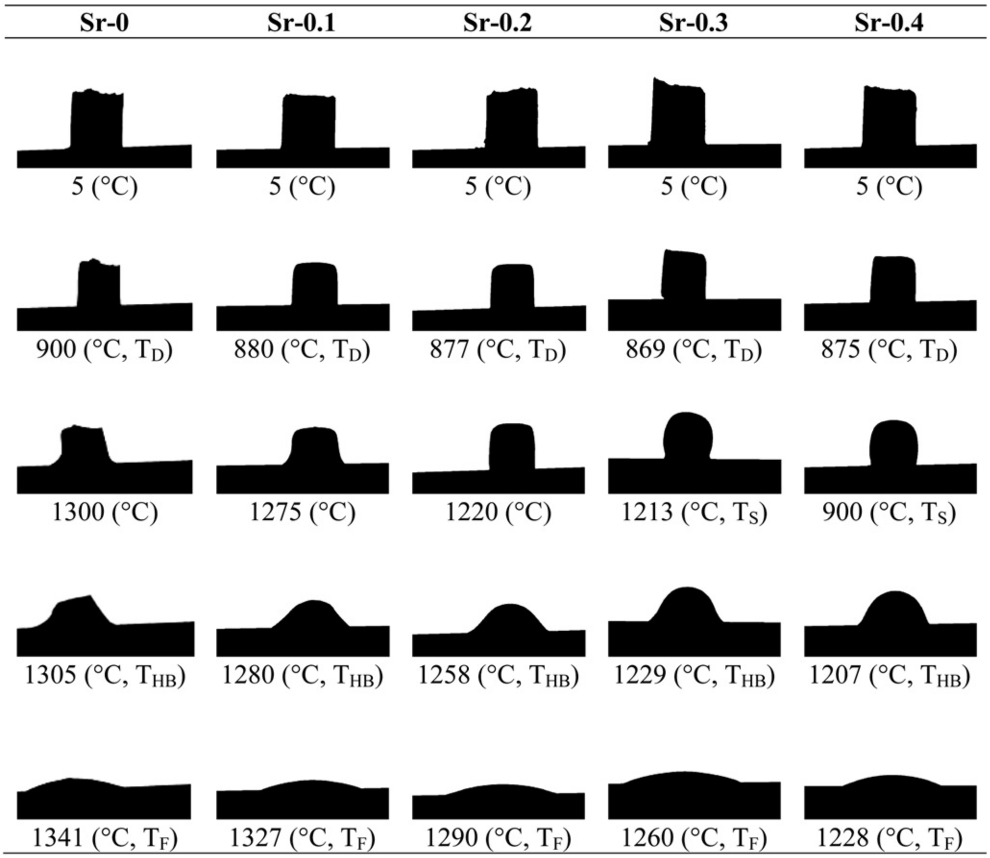

Fig. 4 – HSM images of cylindrical glass-powder compacts on alumina substrate at various stages of heating cycles.

Table 4 – A, B and T_0 constants of the VFT equation, calculated from linear regression analysis, and viscosity at 900 °C.

Glass	A	B	T_0	Log η (dPa s) at 900 °C
Sr-0	0.07	2182	773	6.5
Sr-0.1	0.38	1797	809	6.3
Sr-0.2	0.32	1735	824	6.3
Sr-0.3	0.15	1794	821	6.2
Sr-0.4	0.14	1667	846	6.2

precedes crystallization. This feature will ensure production of well sintered and mechanically strong glass powder compacts. The second stage of densification occurred in competition with crystallization but ended very close to T_p, i.e. peak temperature of crystallization.

3. The values of sintering ability S_c for the SrO containing glasses varied in the interval 19–35 °C and those are considerably higher compared to SrO-free parent glass ($S_c = 7$ °C).
4. The DTA thermographs of the experimental glasses exhibited single crystallization exothermic curve. This signifies that the glass–ceramic is formed either as a result of single phase crystallization or of an almost simultaneous precipitation of more than one crystalline phase. Moreover, values of T_c and the peak temperature of crystallization (T_p) exhibited a tendency to increase with increasing strontium content in the glasses.
5. Fig. 4 presents the photomicrographs of all the investigated glasses depicting the changes in geometric shape of the glasses with respect to temperature as obtained from HSM. The deformation temperature (T_d) of the glasses show linear trend to decrease from 900 to 855 °C with introduction SrO.
6. SrO content in the glasses significantly influenced on the half-ball (T_{HB}) and flow (T_F) temperatures. With increasing SrO content T_{HB} and T_F reduced from 1305 to 1207 °C and from 1341 to 1228 °C, respectively.
7. Values of A/A_0 ranged from 0.64 to 0.71 (Table 3) implying toward good densification level (95–98%) [20].

Fig. 5 represents the viscosity curves for the present investigated glasses measured by least squares fitting of HSM characteristic points using the Vogel–Fulcher–Tammann (VFT) relation $\log \eta = A + B/(T - T_0)$ [18,19,22] where η is the viscosity and T is the temperature. The coefficients A, B and T_0 deduced from the fitting are reported in Table 4.

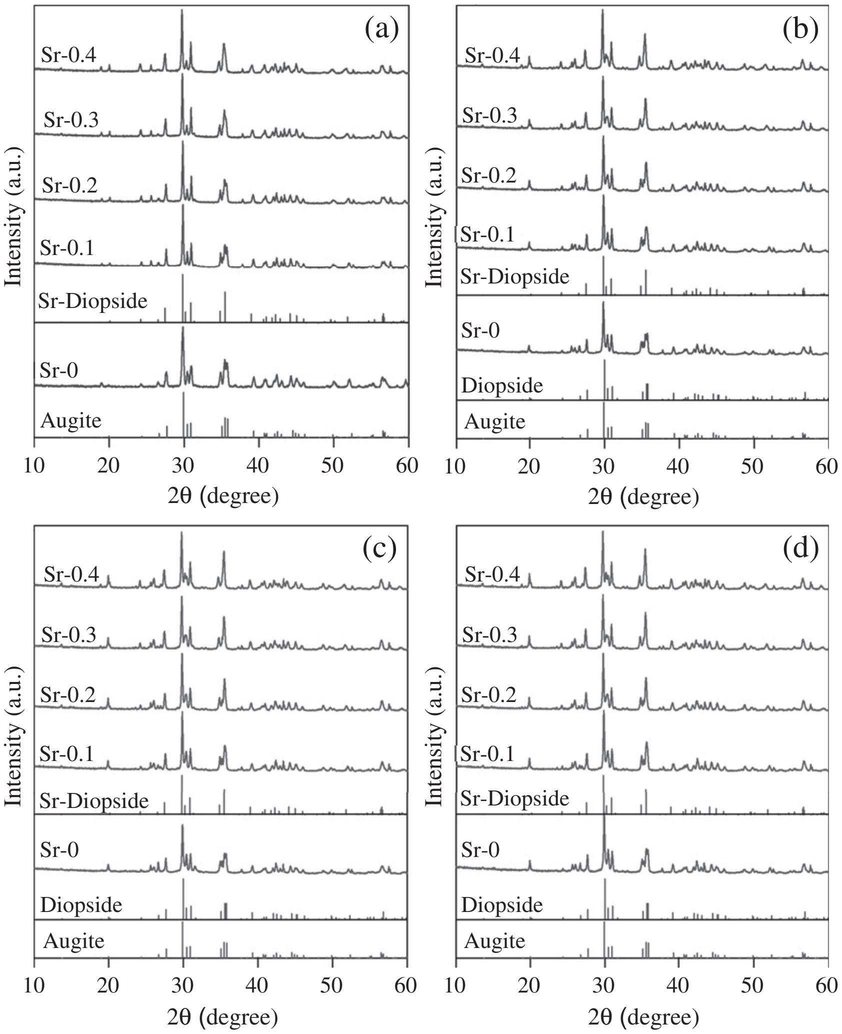

Fig. 6 – XRD pattern of glass–ceramics sintered at 900 °C for: (a) 1 h; (b) 250 h; (c) 500 h; and (d) 1000 h.

3.4. *Stability of crystalline phases*

Fig. 6a presents X-ray diffractograms of the sintered glass powder compacts at 900 °C for 1 h depicting the evolution of crystalline phases. Augite ($CaMg_{0.7}Al_{0.6}Si_{1.77}O_6$; ICDD: 78-1392), an aluminous pyroxene derivative of diopside ($CaMgSi_2O_6$) [23] crystallized as the only phase in the Sr-0 glass–ceramics whilst Sr-containing glasses exhibited a tendency to form Sr–diopside first and Augite as a secondary phases. The standard diffraction patterns of Augite ($CaMg_{0.7}Al_{0.6}Si_{1.77}O_6$, ICDD: 78-1392) and Sr–diopside ($Ca_{0.8}Sr_{0.2}MgSi_2O_6$; ICSD: 68178) are also presented for comparison in Fig. 6a.

The evolution of crystalline phases in the glass-powder compacts sintered at 900 °C for 250 h, 500 h and 1000 h is demonstrated in the X-ray diffractograms (Fig. 6b–d). Table 5 presents the qualitative as well as quantitative analysis of the crystalline phases present in all the investigated GCs as obtained from XRD analysis adjoined with Rietveld–R.I.R technique. Fig. 7 shows the measured XRD pattern fits for Sr-0.1 glass–ceramic sintered at 900 °C for 1 h, by using the GSAS EXPGUI software. The calculated diagrams are based on crystallographic structure models, which also take into account specific instrument and sample effects. The parameters of this model have been refined simultaneously using least-squares methods in order to obtain the best fit to all measured data. By least-squares refinement, a so-called figure-of-merit function *R* has been defined, which describes the residual (agreement) between observed and calculated data [24]. It is noteworthy that many different statistical *R* factors have been proposed for judging the quality of a Rietveld refinement. The *R* factors show the mean deviation in accordance with the model used in percent. The "profile *R*-factor", R_p, and "weighted profile *R*-factor", R_{wp}, for all the refinements are well within the limits of experimental accuracy. The difference plots in Fig. 7 not show any significant misfits. The differences between the main peaks of augite and Sr–diopside were due to adjustment difficulties based on the crystalline of the phases.

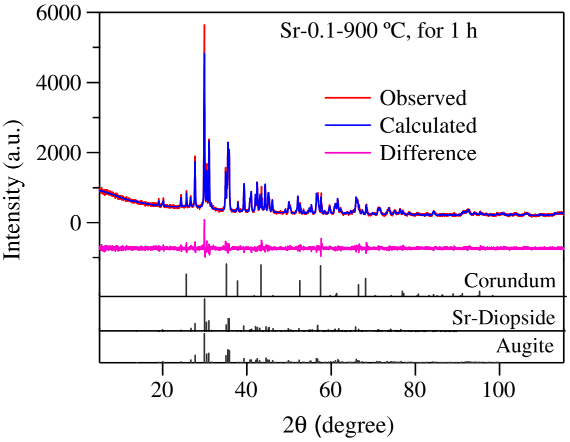

Fig. 7 – Observed, calculated, and difference curve from the Rietveld refinement of the GCs heat treated at 900 °C for 1 h.

In the SrO free glass sintered at 900 °C for 250 h augite crystallized as a major crystalline phase while diopside was the secondary phase (Table 5). Prolonged heat treatment at 500 and 1000 h resulted in diopside as the major and augite as the secondary crystalline phases. Introduction of SrO in the glasses resulted in Sr–diopside formation and suppressing the augite crystallization after sintering at 900 °C for 1 h, 250 h

Table 5 – Results of Rietveld R.I.R. technique.

	Augite	Diopside	Sr–diopside	Amorphous	χ^2
1 h					
Sr-0	95.6	–	–	4.4	3.67
Sr-0.1	24.8	–	59.7	15.5	1.87
Sr-0.2	42.5	–	36.9	20.6	2.35
Sr-0.3	15.2	–	64.5	15.3	2.52
Sr-0.4	22.1	–	61.6	16.3	2.74
250 h					
Sr-0	76.3	21.0	–	2.7	3.86
Sr-0.1	92.4	–	5.6	2.0	3.63
Sr-0.2	13.6	–	78.7	7.7	5.52
Sr-0.3	7.3	–	87.3	5.4	4.87
Sr-0.4	10.0	–	82.3	7.7	5.90
500 h					
Sr-0	10.5	87.5	–	2.0	4.37
Sr-0.1	13.3	–	80.8	5.9	4.73
Sr-0.2	15.1	–	76.3	8.6	6.05
Sr-0.3	–	12.0	81.3	6.6	5.7
Sr-0.4	–	10.3	82.9	6.8	5.8
1000 h					
Sr-0	13.2	86.5	–	0.3	3.89
Sr-0.1	–	69.4	9.4	21.2	5.38
Sr-0.2	–	91.0	8.2	0.8	6.59
Sr-0.3	–	79.3	10.8	9.9	7.14
Sr-0.4	–	9.6	76.7	13.7	6.64

Table 6 – Shrinkage (%), density (g cm^{-3}), bending strength (MPa) and CTE (±0.1) × 10^{-6} K^{-1} (200–700 °C) data measured for the glass-powder compacts after sintering at 900 °C for 1 h, 250 h, 500 h and 1000 h.

Composition	1 h	250 h	500 h	1000 h
Shrinkage				
Sr-0	15.8 ± 0.1	15.7 ± 0.5	15.9 ± 0.3	15.3 ± 0.3
Sr-0.1	12.8 ± 0.2	13.9 ± 0.2	13.9 ± 0.4	13.8 ± 0.3
Sr-0.2	12.5 ± 0.3	14.0 ± 0.1	13.7 ± 0.3	13.9 ± 0.2
Sr-0.3	13.7 ± 0.3	14.6 ± 0.1	14.0 ± 0.1	14.2 ± 0.1
Sr-0.4	13.7 ± 0.1	13.8 ± 0.2	14.2 ± 0.2	14.2 ± 0.1
Density				
Sr-0	2.96 ± 0.001	3.08 ± 0.004	3.09 ± 0.005	3.08 ± 0.006
Sr-0.1	3.10 ± 0.006	3.08 ± 0.003	3.09 ± 0.003	3.09 ± 0.002
Sr-0.2	3.15 ± 0.005	3.12 ± 0.001	3.14 ± 0.006	3.13 ± 0.002
Sr-0.3	3.23 ± 0.007	3.22 ± 0.004	3.22 ± 0.005	3.21 ± 0.002
Sr-0.4	3.25 ± 0.001	3.22 ± 0.002	3.23 ± 0.005	3.23 ± 0.005
Bending strength				
Sr-0	172 ± 4	162 ± 7	161 ± 9	156 ± 8
Sr-0.1	160 ± 5	158 ± 4	154 ± 1	150 ± 4
Sr-0.2	150 ± 7	141 ± 3	150 ± 7	144 ± 5
Sr-0.3	137 ± 7	125 ± 3	133 ± 5	133 ± 8
Sr-0.4	125 ± 3	123 ± 4	122 ± 3	115 ± 3
CTE				
Sr-0	10.4	9.2	10.4	9.60
Sr-0.1	10.8	10.6	10.0	10.1
Sr-0.2	10.2	10.8	9.8	10.8
Sr-0.3	11.2	9.9	10.0	10.4
Sr-0.4	10.3	10.5	10.4	10.7

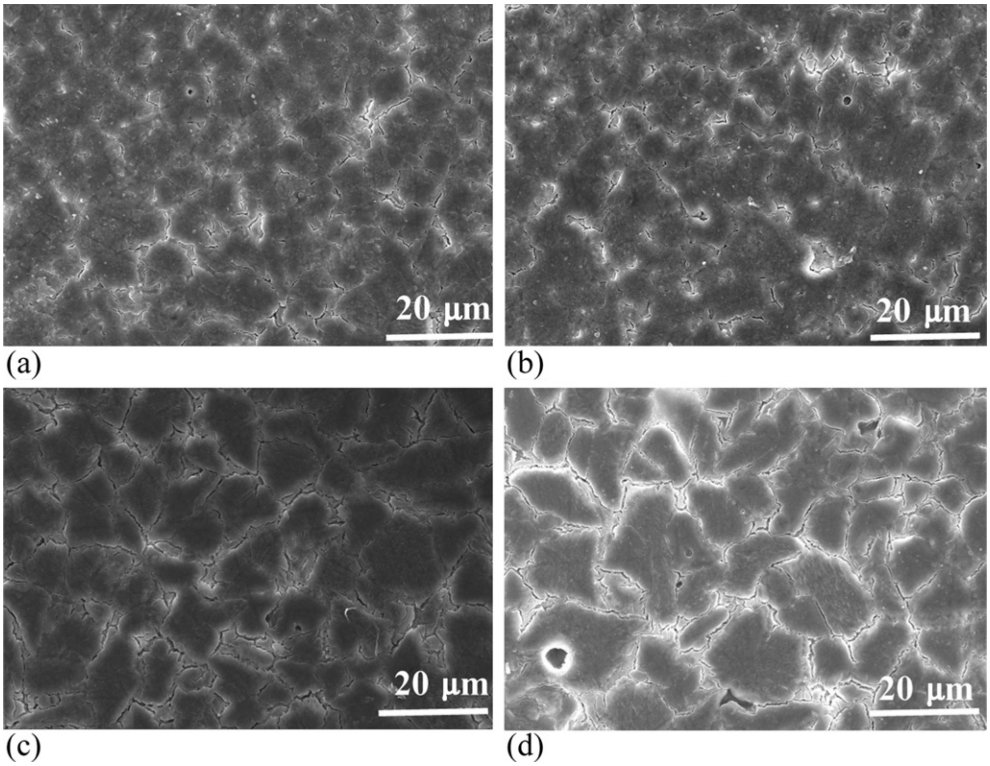

Fig. 8 – Microstructure (revealed via SEM imaging of polished surfaces after chemical etching with 2 vol.% HF solution) of the glass–ceramics heat treated at 900 °C for 1 h in humidified atmosphere: (a) Sr-0.1; (b) Sr-0.2; (c) Sr-0.3; and (d) Sr-0.4.

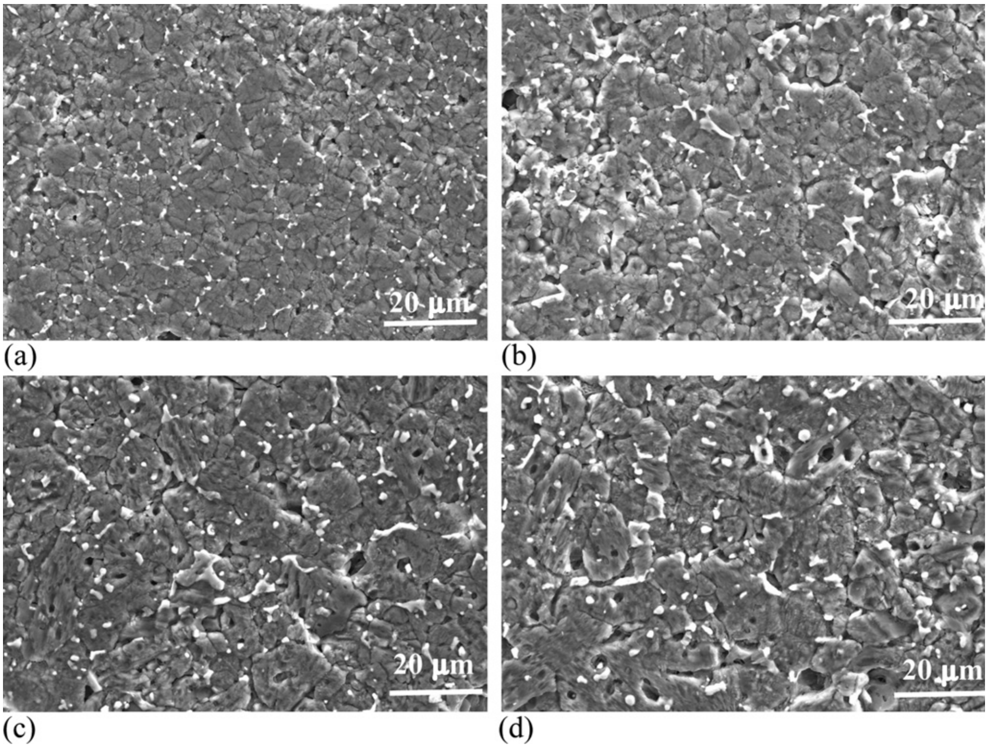

Fig. 9 – Microstructure (revealed via SEM imaging of polished surfaces after chemical etching with 2 vol.% HF solution) of the glass–ceramics heat treated at 900 °C for 1000 h in air atmosphere: (a) Sr-0.1; (b) Sr-0.2; (c) Sr-0.3; and (d) Sr-0.4.

and 500 h. Diopside was the major crystalline phase in the glass-powder compacts Sr-0, Sr-0.1, Sr-0.2 and Sr-0.3 sintered at 900 °C for 1000 h. Only in Sr-0.4 Sr–diopside was crystallized as the primary crystalline phase whilst diopside was the secondary phase. Irrespective of sintering time, increasing SrO content in the glasses initiated growth of the glassy phase in all the glass–ceramics. The residual glassy phase is highest for glass–ceramics Sr-0.2 (20.6 wt.% for 1 h, 7.7 wt.% for 250 h, and 8.6 wt.% for 500 h) and Sr-0.1 glass (21.2 wt.% for 1000 h). Sintered glass–ceramics Sr-0 contain the lowest amount of glassy phase except samples sintered at 900 °C for 250 h.

3.5. *Glass–ceramic properties*

To study variation of glass–ceramic properties namely shrinkage, density, and bending strength glass-powder compacts were sintered systematically at 900 °C for 1 h, 250 h 500 h and 1000 h. According to the values summarized in Table 6 well sintered, dense GCs were obtained after sintering of glass powders at 900 °C for various hours that evidenced from the SEM images of GCs (Figs. 8 and 9). Usually, glass powders in which crystallization precedes sintering result in porous and mechanically weak glass–ceramics exhibit a small shrinkage. In the present scenario, the values of shrinkage varied between 12.5% and ~16% and confirm the good densification of glass powder compacts. Shrinkage decreases after first addition of SrO in the parent glass and then increases reaching the maximum for Sr-0.4 composition. In general, SrO-free parent composition exhibited the highest value of shrinkage among investigated compositions independent on the dwell time.

The density values of glass–ceramics are well correlated with the density of respective bulk glasses and increased with increasing SrO content. Fig. 10a represents the mechanical strength of the produced glass–ceramics with respect to the sintering time. In general, bending strengths of the glass–ceramics decreased with increasing SrO and as well as sintering time that may be due to the formation of higher amount of residual glassy phase (Table 5). Thus, the glass–ceramics Sr-0 glasses attained maximum bending strength values varied between 156 and 172 MPa whilst Sr-0.4 glass–ceramics demonstrates minimum values of 125–115 MPa. However, compared to parent (SrO-free) GCs SrO-containing compositions exhibited remarkable stability in retaining mechanical strength after prolonged heat treatments. Thus, after 1000 h heat treatment at 900 °C decrease in bending strength attained 9.3% for Sr-0, 6.3% for Sr-0.1, 4.0%, for Sr-0.2, 2.9%, for Sr-0.3 and 4.8% for Sr-0.4.

The CTE values of the glass–ceramics sintered at 900 °C for 1 h, 250 h, 500 h and 1000 h are presented in Table 6. As complimentary Fig. 10b represents the line art for the variation of CTE of the produced GCs with respect to the sintering time. Sr-0.3 glass–ceramic exhibited highest CTE (11.2×10^{-6} K^{-1}) among GCs sintered at 900 °C for 1 h. No significant changes in thermal expansion were observed in SrO-containing GCs after long heat treatment at 900 °C for 1000 h compared to the parent GCs. Except for Sr-0 heat treated for 250–1000 h and Sr-0.3 sintered for 1 h, the CTE values vary in the narrow range of $(9.8–10.8) \times 10^{-6}$ K^{-1}, which are compatible with those of common SOFC components. If compared to the thermal expansion of stabilized zirconia solid electrolytes and SOFC interconnects (e.g., see Refs. [2,3,12] and references therein), the differences in CTEs are lower than 5–6%.

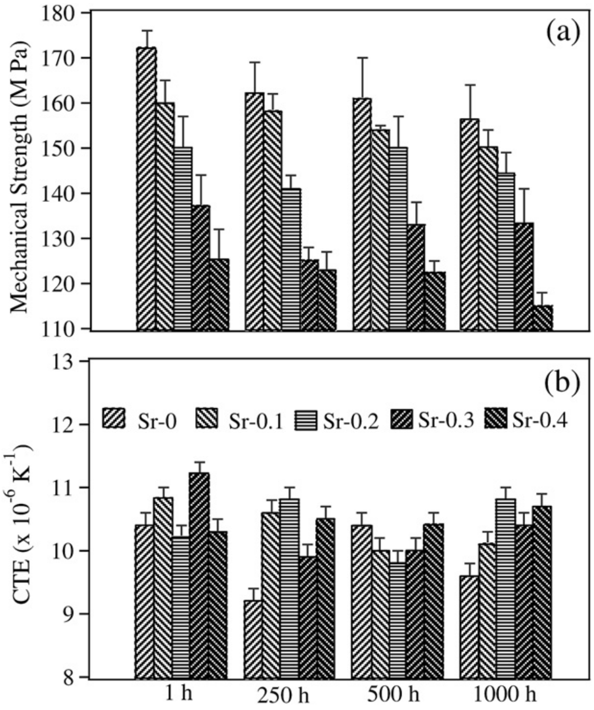

Fig. 10 – Variations in mechanical strength and CTE in glass–ceramics sintered at 900 °C for various time periods ranging from 1 to 1000 h.

3.6. *Interaction studies*

All the glass–ceramic seals bonded well to Sanergy HT metallic interconnect as well 8YSZ ceramic plate, no gaps were observed, and the investigated interfaces showed homogeneous microstructures over their entire cross-sections of the joint. Figs. 11a and 12a show the SEM image of the interfaces between Sanergy HT/glass–ceramic and 8YSZ/glass–ceramic for Sr-0.3 glasses, along with the corresponding EDS mappings of the relevant elements existing at the interface after heat treatment at 900 °C for 1 h in air. Figs. 11b and 12b present the elemental distribution profiles for Cr, Fe, Mn, Ni, Ba, La, Ca, Ti, Si, Al and Sr elements along the interface of Sr-0.3/Sanergy HT and Y, Zr, Ba, La, Ca, Si, Al and Sr along the interface of Sr-0.3/8YSZ. Neither diffusion layers were detected at the interfaces by SEM/EDS analyses (Fig. 11c–f), within the limits of experimental uncertainty. However, long term thermal stability of these couples and their behavior during the SOFC startup/shutdown regimes are yet to be investigated. In particular, electron microscopic analysis revealed the formation of thin interfacial layers on heating up to 1000 °C. As an example, Fig. 13 compares two fractured interfaces between 8YSZ ceramics and Sr-0.3 sealant, sintered at 900 °C (A) and 1000 °C (B) during 30 min. The interaction visible at 1000 °C may be associated with alkaline-earth zirconate formation promoted in the presence of liquid phase. Whatever the microscopic mechanisms, phase formation at the sealant/electrolyte interface may

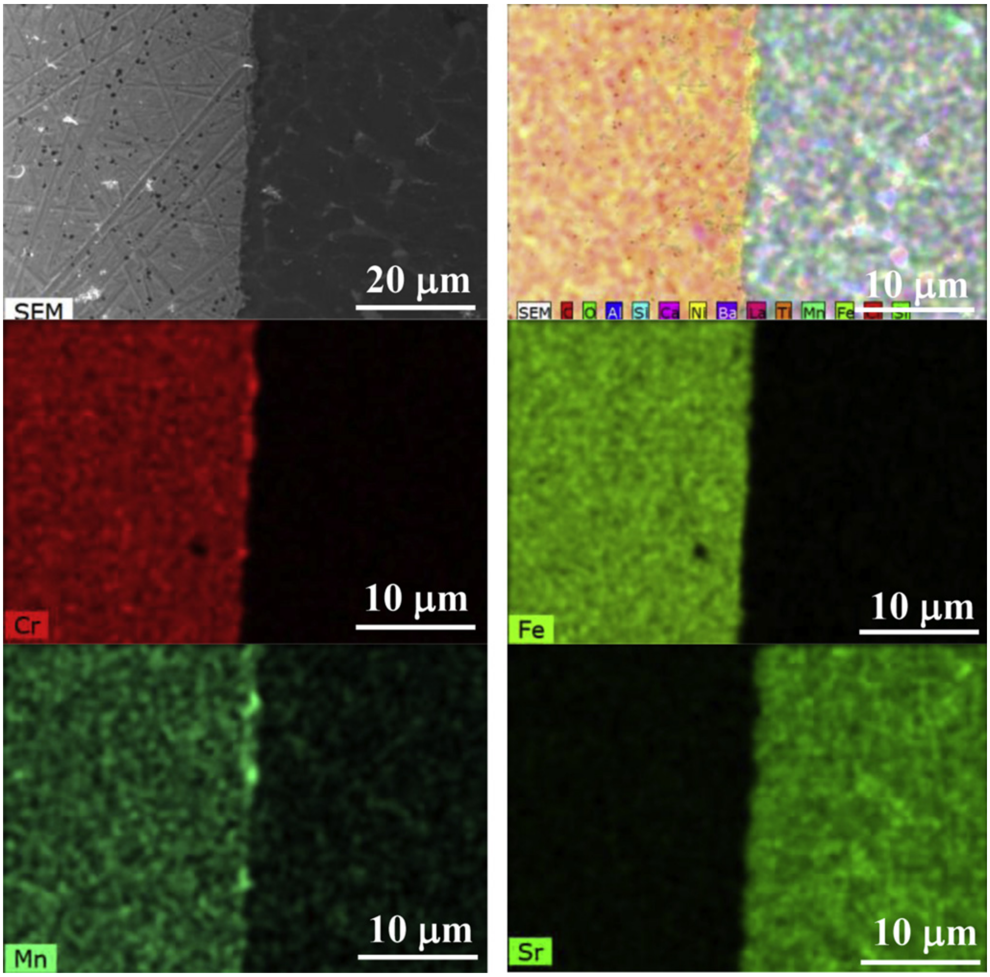

Fig. 11 – SEM image and EDS element mappings for Cr, Fe, Mn and Sr at the interface between Sr-03 and Sanergy HT after heat treatment at 900 °C for 1 h.

lead to worse thermomechanical stability and should hence be avoided by optimizing the SOFC fabrication and operation regimes; the latter is also necessary to suppress cation interdiffusion between other SOFC components. The results on electrical resistivity of the Sr-0.3/8YSZ diffusion couples showed that no time degradation occurs at the SOFC operation temperatures, such as 800 °C. One example is presented in Fig. 14a; except for data scattering associated with high resistivity of the glass–ceramic sealant (±2%), the electrical resistance exhibits no changes with time, within the limits of experimental error.

3.7. *Electrical properties of the sealants*

For all studied glass–ceramics, the Arrhenius dependencies of the total conductivity (Fig. 15) are linear, confirming that no phase changes take place after sintering at 900 °C. Increasing strontium concentration leads to a higher conductivity, whilst the activation energy decreases from 246 ± 7 down to 162 ± 3 kJ mol^{-1} (Fig. 16). Nonetheless, all the sealants possess excellent insulating properties; in the temperature range necessary for SOFC operation; their electrical resistivity is higher than 2 MOhm cm. The linear relationship between the molar volume and conductivity activation energy (inset in Fig. 16) may suggest a dominant role of ionic charge carriers. Indeed, the ion transference numbers estimated by the electromotive force (EMF) method under air/10% H_2–90% N_2 gradient were found close to unity within the limits of experimental uncertainty. In accord with the very high level of the electrical resistance, this finding shows that NiO additive provides no significant electronic contribution to the conductivity. Although the EMF technique makes it impossible to determine the type of ionic charge carriers, the conductivity does not change when hydrogen or water vapor are present in the gaseous phase (Fig. 14b), thus indicating that protonic contribution is negligible. Furthermore, the oxygen permeation tests revealed no leakage fluxes through sintered gas–ceramics, again in agreement with their high electrical resistivity.

4. Discussion

A choice of an appropriate glass–ceramic sealant material is essential for developing reliable planar SOFCs. In this regard special attention was drawn to CTE of a parent glass that

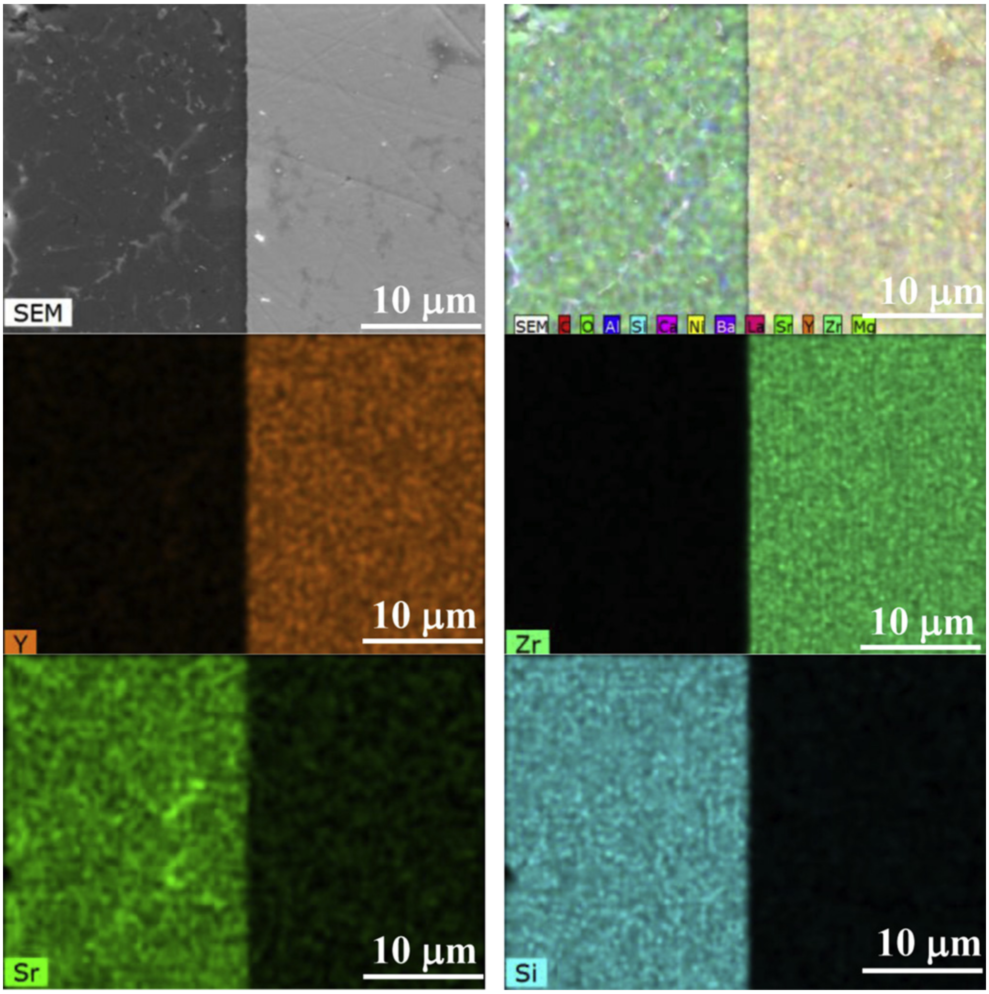

Fig. 12 – SEM image and EDS element mappings for Y, Zr, Sr, and Si at the interface between Sr-0.3 and 8YSZ after heat treatment at 900 °C for 1 h.

should be nearly equal to CTE of respective crystallized material. This would ensure appropriate adhesion of glass powder to anode, cathode and interconnect material during cell stack sealing procedure. Another critical issue is achieving stability GC's phase composition at prolonged heat treatment to get mechanical integrity of a pSOFC stack at operating conditions. Thus, an effect of different lanthanides (La, Nd, Gd and Yb) to tailor CTE and viscosity of alkaline-earth aluminosilicate glass–ceramic seals composition was recently investigated [4]. The electrical conductivity of the investigated glass–ceramics varied in the range (1.2–7.3) × 10^{-7} S cm^{-1} (750–800 °C) while the CTE was (9.4–11.2) × 10^{-6} K^{-1}

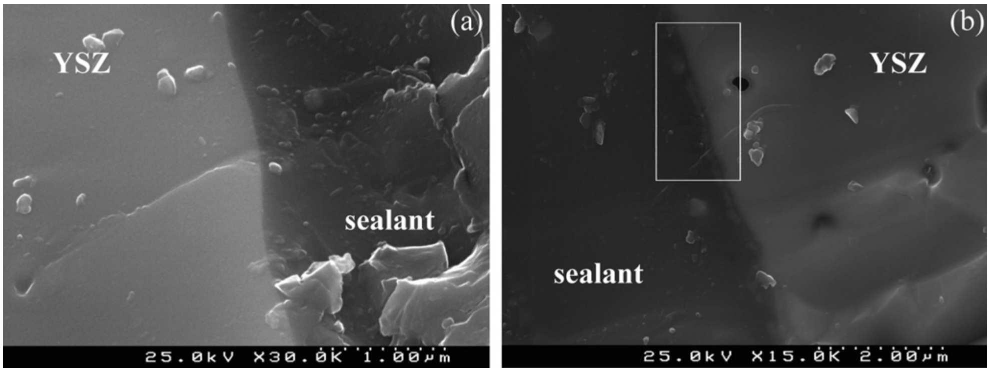

Fig. 13 – SEM micrographs of fractured Sr-0.3/8YSZ interfaces after sintering (a) 900 °C and (b) 1000 °C during 30 min.

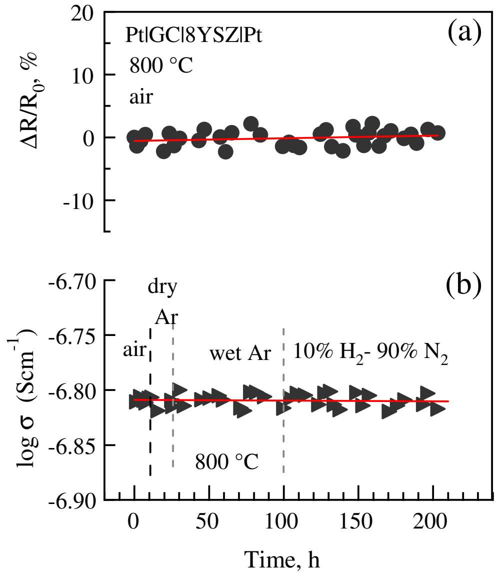

Fig. 14 – Time dependencies of the relative variations of electrical resistance of Sr-0.3/8YSZ couple (a) in air and (b) total conductivity of Sr-0.3 glass–ceramics in various atmospheres, at 800 °C.

(200–700 °C). However, further experimentation with respect to their thermal stability under long term testing was needed in order to prove their efficacy [4].

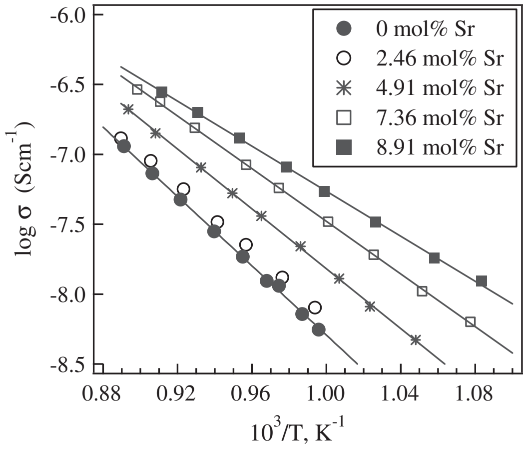

Fig. 15 – Temperature dependencies of the total electrical conductivity in atmospheric air.

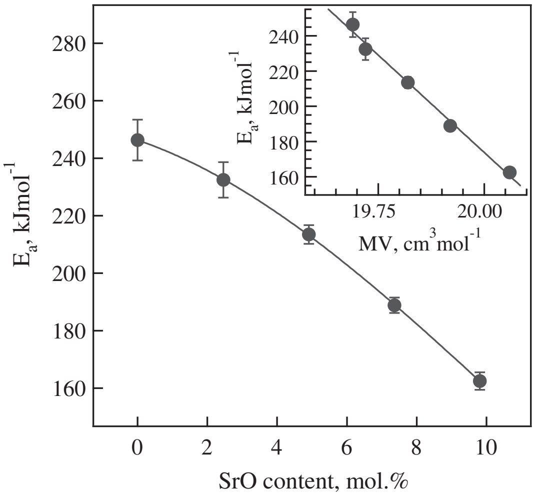

Fig. 16 – Activation energy for the electrical conductivity of the studied glass–ceramics inset shows the relationship between the total conductivity activation energy and molar volume.

In the present study via systematic substitution of SrO for CaO in pyroxene structure, a new challenge was undertaken to tailor CTE of parent glass and crystallized material as well as to stabilize thermo-mechanical properties of GCs. Analysis of glass properties demonstrated that CTE significantly increased at first addition of SrO reaching the maximum when Sr replaced 20 and 30% of Ca with some decline at further SrO increment (Table 2). The CTE values for SrO-containing glasses varied in the interval (10.0–11.3) × 10^{-6} K^{-1} indicating that Sr for Ca substitution in pyroxene glasses enhances the CTE. This effect can be explained by the differences in bond lengths of Ca–O (2.38 Å) and Sr–O (~2.60 Å) groups [25]. Regarding the density of glasses, the values changed from 2.990 to 3.167 g cm^{-3}, with minimum and maximum values being registered for the parent and Sr-0.4 glass compositions, respectively (Table 2), i.e. variations are composition dependent and can be explained by atomic weight considerations. Due to the larger size of Sr ions (1.32 Å) as compared to Ca ions (1.14 Å), the substitution of SrO for CaO results in a larger cell volume and consequently large molar volume of the glasses. Sr is heavier than Ca (with atomic weights of 87.62 and 40.078 g mol^{-1}, respectively) and, therefore, the weight of the cell also increases with the increasing substitution of SrO in the glasses. In the present case, the increase in cell weight seems to dominate over the increase in cell volume, leading to higher density values for the SrO-substituted glasses.

T_g as a parameter related to the system viscosity [26], decreased in all the investigated SrO-containing compositions when compared to the parent glass (Table 3, Fig. 1). In general, strontium is a slightly larger ion than calcium, thus its incorporation expands the glass network and lowers the energy barrier for the glass to super cooled liquid transition, which results in T_g drop. Earlier Fujikura et al. [27] revealed non-linear variation T_g with substitution of Sr for Ca while O'Donnell et al. [28] revealed a linear trend. Additionally, incorporation of SrO in the pyroxene glasses reduced the viscosity of glasses close to ~10^6 dPa s at 900 °C (Fig. 5, Table 4). This is a quite decisive factor since within the temperature range of 850–900 °C that is usually considered for joining of SOFC metallic/ceramic components by a glass/glass–ceramic sealant [29,30], glass viscosity must be low enough, e.g. ~10^6 dPa s at 900 °C.

With respect of glass structural changes K. Fujikura et al., investigated ^{29}Si MAS–NMR spectra of SrO containing glasses [27] and demonstrated that only 50% Sr for Ca substitution influenced the silicate network. Similarly in the present study ^{29}Si–MAS–NMR and ^{27}Al MAS–NMR spectra revealed no variation in the chemical shifts for silicon and aluminum atoms in all SrO-containing glasses including composition Sr-0.4 with 40% Sr for Ca substitution. Therefore, further substitutions of

Ca for Sr in the pyroxene structure will be attempted to reveal any possible effects occurred in the glass structure.

It was depicting that addition of SrO enhances glass sintering ability considerably. The higher values of S_c (Table 3) correspond to delay in nucleation and thus provide a wider processing window for a glass composition to attain maximum densification. Moreover, characteristic temperatures T_d, T_S, T_{HB} and T_F decreased with increment of SrO (Table 3) that correlates well with the trends observed from the corresponding viscosity curves (Fig. 5).

To minimize thermal stresses during cell operation the differences in CTEs between interconnect and the seal glass should not exceed, in general, 1×10^{-6} K^{-1} [31]. In respect to the CTE variation for glass–ceramics, their thermal expansion behavior depends on the nature and amount of crystalline phase present in the glass–ceramic system. Owing to the formation of stable pyroxene type crystalline phases such as diopside, Sr–diopside and augite, which are solid solutions of $CaMgSi_2O_6$, stability of CTE was achieved under various heat treatment conditions (Table 6). In general, all the studied SrO-containing glass–ceramics exhibited their CTE in the range (9.6–11.2) $\times 10^{-6}$ K^{-1} that are nearly equal to CTE of parent glasses (10–11.3) $\times 10^{-6}$ K^{-1}. Considering CTE values for metallic interconnect (Crofer22 APU; Sanergy HT) varying in the range (11–12) $\times 10^{-6}$ K^{-1}, and ceramic electrolyte (i.e. 8YSZ) to be (10–12) $\times 10^{-6}$ K^{-1} both the parent glasses and corresponding GC composition Sr-0.2, Sr-0.3 and Sr-0.4 (Table 6) should be suitable for rigid glass/glass–ceramic seals. The improved adhesion to Sanergy HT/glass–ceramic and 8YSZ/glass–ceramic for Sr-containing glasses and absence formation of detrimental phases at 900 °C support this conclusion. In combination with the relatively low temperatures of liquid phase formation, such features are advantageous for intermediate-temperature (IT) SOFCs where heating during stack hermetization may lead to passivation of the electrodes and degradation of other components. However, the substantially high concentration of strontium and the concomitant decrease of viscosity may result in a more extensive interaction between zirconia solid electrolytes and sealant, demanding for a careful control of temperature upon SOFC hermetization. Furthermore, long-term thermal stability of these sealants in contact with solid electrolytes and interconnect materials must be investigated.

5. Conclusions

The following conclusion from the present work might be drawn:

1. Strontium for calcium substitution in diopside–Ba disilicate glass–ceramic revealed to be a promising strategy for stabilizing the thermal parameters and enhancing the adhesion of GCs seals to interconnect material of SOFCs.
2. Systematic substitution Sr for Ca in pyroxene structure decreases the viscosity of glasses at temperatures close to T_g and within the range of 850–900 °C that is usually considered for joining of SOFC metallic/ceramic components by a glass/glass–ceramic sealant.
3. All the studied SrO-containing glasses exhibited higher CTE compared to the SrO-free parent glass. Their CTE values varied in the range (10.0–11.3) $\times 10^{-6}$ K^{-1} and are nearly equal to CTE of corresponding GCs (9.6–11.2) $\times 10^{-6}$ K^{-1}. CTE of investigated glass–ceramics are relatively stable under different heat treatment schedules and correlated quite well with those of ceramic electrolyte, 8YSZ and metallic interconnect, Sanergy HT.
4. The sintering precedes crystallization resulting in well sintered and dense glass powder compacts. Although densification occurred in two stages, the first stage contributed in 95–98% to the total shrinkage and was accomplished at T_{MS1}, i.e., before the onset of crystallization.
5. Precipitation and mutual transformation of pyroxene based phases, i.e. solid solutions of diopside, after prolonged isothermal heat treatment was revealed and no formation of other detrimental phases were detected. This feature ensured stability of CTE under various heat treatment conditions.
6. Glass–ceramics demonstrated excellent insulating properties. Their specific electrical resistivity is higher than 5 MOhm cm at 800 °C, and is independent of the oxygen and water vapor partial pressures. This enables isolation between the fuel cell components. No oxygen leakage fluxes through dense glass–ceramics were detected within the limit of experimental error.
7. Homogeneous microstructures over the entire cross-sections of the GC-interconnect joints (a) without gaps formation, (b) no appreciable diffusion of elements from GC toward Sanergy HT and vice-versa, and (c) absence of any detrimental Cr or Ba-rich layers were observed.

Acknowledgment

This study was financially supported by the University of Aveiro, CICECO, and FCT, Portugal (PTDC/CTM–CER/114209/2009 and PEst–C/CTM/LA0011/2011).

REFERENCES

[1] Wachsman ED, Marlowe CA, Lee KT. Role of solid oxide fuel cells in a balanced energy strategy. Energy Environ Sci 2012;5:5498–509.

[2] Mahapatra MK, Lu K. Glass-based seals for solid oxide fuel and electrolyzer cells – a review. Materials Sci Eng R 2010;67:65–85.

[3] Barfod R, Koch S, Liu YL, Larsen PH, Mogensen M, Hendriksen PV. Long-term tests of DK–SOFC cells. Proc Electrochem Soc (SOFC VIII) 2003;7:1158–66.

[4] Goel A, Reddy AA, Pascual MJ, Gremillard L, Malchere A, Ferreira JMF. Sintering behavior of lanthanide-containing glass–ceramic sealants for solid oxide fuel cells. J Mater Chem 2012;22:10042–54.

[5] Donald IW, Mallinson PM, Metcalfe BL, Gerrard LA, Fernie JA. Recent developments in the preparation, characterization and applications of glass and glass–ceramic to metal seals and coatings. J Mater Sci 2011;46:1975–2000.

[6] Zhang T, Brow RK, Fahrenholtz WG, Reis ST. Chromate formation at the interface between a solid oxide fuel cell glass and interconnect alloy sealing. J Power Sources 2012;205:301–6.

[7] Goel A, Tulyaganov DU, Kharton VV, Yaremchenko AA, Ferreira JMF. The effect of Cr_2O_3 addition on crystallization

and properties of La_2O_3-containing diopside glass–ceramics. Acta Materialia 2008;56:3065–76.

[8] Goel A, Shabban ER, Tulyaganov DU, Ferreira JMF. Study of crystallization kinetics in glasses along the diopside–Ca–Tschermak join. J Am Ceram Soc 2008;91:2690–7.

[9] Goel A, Pascual MJ, Ferreira JMF. Stable glass–ceramic sealants for solid oxide fuel cells: influence of Bi_2O_3 doping. Int J Hydrogen Energy 2010;35:6911–23.

[10] Goel A, Tulyaganov DU, Kharton VV, Yaremchenko AA, Ferreira JMF. Electrical behavior of aluminosilicate glass–ceramic sealants and their interaction with metallic solid oxide fuel cell interconnects. J Power Sources 2010;195:522–6.

[11] Reddy AA, Tulyaganov DU, Goel A, Pascual MJ, Kharton VV, Tsipis EV, et al. Diopside–Mg orthosilicate and diopside–Ba disilicate glass–ceramics for sealing applications in SOFC: sintering and chemical interactions studies. Int J Hydrogen Energy 2012;37:12528–39.

[12] Fergus JW. Sealants for solid oxide fuel cells. J Power Sources 2005;147:46–57.

[13] Ojha PK, Rath SK, Chongdar TK, Gokhale NM, Kulkarni AR. Physical and thermal behaviour of Sr–La–Al–B–Si based SOFC glass sealants as function of SrO content and B_2O_3/SiO_2 ratio in the matrix. J Power Sources 2011;196:4594–8.

[14] Kumar V, Arora A, Pandey OP, Singh K. Studies on thermal and structural properties of glasses as sealants for solid oxide fuel cells. Int J Hydrogen Energy 2008;33:434–8.

[15] Mahapatra MK, Lu K. Sealing evaluation of an alkaline earth silicate glass for solid oxide fuel/electrolyser cells. Fuel Cells 2011;11:436–44.

[16] Kaur G, Pandey OP, Singh K. Interfacial study between high temperature $SiO–B_2O_3–AO–La_2O_3$ (A = Sr, Ba) glass seals and Crofer22APU for solid oxide fuel cell applications. Int J Hydrogen Energy 2012;37:6862–74.

[17] Sharma K, Kothiyal GP, Montagne L, Mear FO, Revel B. A new formulation of barium–strontium silicate glasses and glass–ceramics for high-temperature sealant. Int J Hydrogen Energy 2012;37:11360–9.

[18] Scholze H. Influence of viscosity and surface tension on hot-stage microscopy measurements on glasses. Ver Dtsch Kerom Ges 1962;391:63–8.

[19] Pascual MJ, Duran A, Prado MO. A new method for determining fixed viscosity points of glasses. Phys Chem Glasses 2005;46:512–21.

[20] Pascual MJ, Kharton VV, Tsipis EV, Yaremchenko AA, Lara C, Durán A, et al. Transport properties of sealants for high temperature electrochemical applications: $RO–BaO–SiO_2$ (R = Mg, Zn) glass–ceramics. J Eur Ceram Soc 2006;26: 3315–24.

[21] Goel A, Tulyaganov DU, Pascual MJ, Shaaban ER, Munoz F, Lü Z, et al. Development and performance of diopside based glass–ceramic sealants for solid oxide fuel cells. J Non-cryst Solids 2010;356:1070–80.

[22] Reinsch S, Luis M, Nascimento F, Müller R, Zanotto ED. Crystal growth kinetics in cordierite and diopside glasses in wide temperature ranges. J Non-cryst Solids 2008;354: 5386–94.

[23] Goel A, Tulyaganov DU, Agathopoulos S, Ribeiro MJ, Ferreira JMF. Crystallization behaviour, structure and properties of sintered glasses in the diopside–Ca–Tschermak system. J Eur Ceram Soc 2007;27: 3231–8.

[24] Young RA. The Rietveld method. International union of crystallography monographs on crystallography. In: Young RA, editor. Introduction to Rietveld method, vol. 50. Oxford: Oxford University Press; 1993. p. 1–39.

[25] Xiang Y, Du J. Effect of strontium substitution on the structure of 45S5 bioglasses. Chem Mater 2011;23:2703–17.

[26] Nascimento MLF, Aparicio C. Viscosity of strong and fragile glass-forming liquids investigated by means of principal component analysis. J Phy Chem Solids 2007;68:104–10.

[27] Fujikura K, Karpukhina N, Kasuga T, Brauer DS, Hill RG, Law RV. Influence of strontium substitution on structure and crystallisation of bioglass 45S5. J Mater Chem 2012;22: 7395–402.

[28] O'Donnell MD, Candarlioglu PL, Miller CA, Gentleman E, Stevens MM. Materials characterisation and cytotoxic assessment of strontium-substituted bioactive glasses for bone regeneration. J Mater Chem 2010;20:8934–41.

[29] Smeacetto F, Salvo M, Ferraris M, Cho J, Boccaccini AR. Glass–ceramic seal to join Crofer 22 APU alloy to YSZ ceramic in planar SOFCs. J Eur Ceram Soc 2008;28:61–8.

[30] Chou YS, Stevenson JW, Gow RN. Novel alkaline earth silicate sealing glass for SOFC part II. Sealing and interfacial microstructure. J Power Sources 2007;170:395–400.

[31] Kirsch R. Glass science and technology, vol. 13. Amsterdam: Elsevier; 1993. p. 352.